Catalysis Today xxx (xxxx) xxx–xxx

Contents lists available at ScienceDirect

Catalysis Today

journal homepage: www.elsevier.com/locate/cattod

Stability of mesocellular foam supported copper catalysts for methanol synthesis

C.E. Pompe[a,1], D.L. van Uunen[a], L.I. van der Wal[a], J.E.S. van der Hoeven[a,b], K.P. de Jong[a], P.E. de Jongh[a,*]

[a] Inorganic Chemistry and Catalysis, Debye Institute for Nanomaterials Science, Utrecht University, Universiteitsweg 99, 3584 CG, Utrecht, the Netherlands
[b] Soft Condensed Matter, Debye Institute for Nanomaterials Science, Utrecht University, Princetonplein 5, 3584 CC, Utrecht, the Netherlands

ARTICLE INFO

Keywords:
Mesocellular foam
Mesoporous silica
Copper catalysts
Methanol synthesis
Catalyst stability

ABSTRACT

Mesocellular foam is a well-defined mesoporous silica comprising large cages (~20 nm), connected by small windows (2–10 nm). Here, we used mesocellular foam as a support material in the preparation of Cu based model catalyst for methanol synthesis at high temperature and pressure. To this end, we synthesized two types of mesocellular foam, with the same cage size, but a different window size of 8 and 2.3 nm, and compared them to the use of a silica gel support. Cu particles were deposited by impregnation with a copper nitrate precursor solution and decomposition in either N_2 or H_2-containing gas stream. We followed the phase evolution *in situ*, and identified a method using direct reduction in H_2 to deposit 3 nm Cu particles on all different supports. The catalysts prepared on the mesocellular foam displayed a much higher stability than the silica gel supported catalysts. The impact of the window size of the MCF was small, but significant: the catalysts supported on the small window mesocellular foam were more stable on the long term. However, they also had a lower activity due to embedment of the Cu particles in the windows, as revealed with electron tomography. A higher metal loading on the small window mesocellular foam resulted in enhanced coalescence of the Cu particles, which was attributed to smaller interparticle distances. Increasing the loading on this support even further increased the size and polydispersity of the Cu nanoparticles, leading to a higher deactivation rate due to Ostwald ripening. Hence, the loading and size polydispersity are important parameters in determining the catalyst stability. We also found that the nature of the SiO_2 support has more impact on the catalyst stability than the restricting pore sizes, probably due to the fact that Ostwald ripening dominates particle growth on the longer time scales.

1. Introduction

Heterogeneous catalysts often comprise metals supported on metal oxides, the latter to provide anchoring and stability for the active metal nanoparticles. High surface area silica is easy to prepare, porous 3D structures can be varied and hence it is used frequently for fundamental research. Silica is also inert and therefore does not influence most chemical reactions. A few well-studied examples are the ordered mesoporous structures MCM-41 [1–3], SBA-15 [4] and SBA-16 [5] and the more disordered structure MCF [4,6,7].

The latter, MCF (mesocellular foam) was first proposed in 1999 [6]. It has large (15–30 nm) cages, connected by small (~10 nm) windows [6]. The structure is very suitable to host biocatalysts such as enzymes [8], metal-organic complexes [9] and heterogeneous catalysts. Metal organic complexes or organic molecules are often grafted onto the SiO_2 to improve the recyclability of the catalysts [10–12]. Grafting is not necessary if the window size is decreased to 2–5 nm, the size of large organic molecules. This has been achieved by modifying the existing synthesis procedure of MCF [9]. A [Co(salen)] complex was synthesized by a ship-in-a-bottle approach in the cages of this so-called modified-MCF (m-MCF) [9], leading to improved activity, stability and catalyst recovery compared to the corresponding free homogeneous catalyst [9].

In heterogeneous catalysis, MCF has been investigated to support for instance Co [13] for the Fischer-Tropsch reaction and Pt for the reforming of n-hexane [14], where in both cases MCF was used as model support. MCF supported Cu_2O nanoparticles were used for the photocatalytic evolution of H_2 from H_2O [15], and Au for the liquid phase oxidation of 5-hydroxymethyl furfural [16], where the MCF contributed to a higher catalyst stability. Ni/MCF has been used for the production

* Corresponding author.
E-mail address: P.E.deJongh@uu.nl (P.E. de Jongh).
[1] Current address: RIVM, National Institute for Public Health and the Environment, Antonie van Leeuwenhoeklaan 9, 3721 MA Bilthoven, the Netherlands.

https://doi.org/10.1016/j.cattod.2019.01.053
Received 13 July 2018; Received in revised form 16 January 2019; Accepted 21 January 2019

of hydrogen from the pyrolysis of glucose [17], the MCF enabled a higher efficiency of the catalyst. Maghemite (γ-Fe_2O_3) particles have been synthesized in MCF to act as precursor for a variety of catalysts and reactions [18], which were easy to recover. MCF supported Pd catalyst have been used for a variety of reactions, including decarboxylation of stearic acid [19], the racemization of amines [20], oxidation of alcohols [21], the hydrogenation of phenylacetylene [22] and the Suzuki cross-coupling reaction [23]. The MCF support led to better recoverability or higher activity and selectivity of these Pd catalysts.

The size of the small 2–5 nm windows in MCF, suitable for entrapping metal-organic complexes, is also in the range of nanoparticles used in heterogeneous catalysis. The deposition of metal nanoparticles, being slightly larger than the windows, in the cages of the modified-MCF, could restrict the particles from moving to neighboring cages. Limited movement in space lowers the chance of coalescence with nanoparticles in other cages, as shown for confinement of SiO_2 supported catalysts before [16,24–29]. This lower extent of coalescence and therefore less particle growth can provide stability of the catalyst [30–32]. For CuZn/SiO_2 catalysts for methanol synthesis it has been shown that decreasing the pore size of a non-cage-like SiO_2 improves the stability [33]. Moreover, by placing the CuZn particles in the cage-like SiO_2 SBA-16 the stability of these catalysts can be improved by narrowing the window size [34]. Furthermore the chance of coalescence can be decreased by increasing the interparticle distance [35]. Growth of the nanoparticles can also occur *via* Ostwald ripening. The rate of Ostwald ripening depends on the polydispersity of the nanoparticles and can be slowed down by a narrow particle size distribution [36–38].

To study particle growth as deactivation mechanism, methanol synthesis from syngas ($CO/CO_2/H_2$) is an excellent model reaction. Cu/ZnO/Al_2O_3 is generally used in industry as catalyst for this process, which runs at high pressures (50–100 bar) and temperatures (210–290 °C) [39,40]. The catalyst suffers from deactivation by particle growth of the Cu nanoparticles and/or loss of the Zn promoter efficiency [35,41–44]. This reaction has a very high selectivity (> 99%) towards methanol and hardly any other deactivation mechanisms than particle growth play a role in the loss of activity [41,45]. No coke is formed on the Cu surface and since silica is inert, strong metal support interactions do not play a role [46,47].

We chose to use only Cu, without Zn-species as promoter, to ensure that the activity evolution of the catalysts can be directly related to particle growth. However, there are more factors which might influence the activity of a catalyst, such as blocking of the metallic surface area when particles are located in small pores and the particle size effect where particles larger than 6 nm display a higher turn-over-frequency (TOF) than smaller particles [31,48]. One of the few systems for which this particle size effect is known in detail is Cu/SiO_2, and therefore can be taken into account [48].

Studying Cu nanoparticles in the MCF structure with large and small windows allows insight in the deactivation and particle growth mechanisms of this type of metal nanoparticle catalysts. We chose to use direct reduction in H_2 of the impregnated $Cu(NO_3)_2$ phase [49] and achieved homogeneous distributions of Cu particles on large window MCF, small window m-MCF as well as for a silica gel (a non-cage-like material). This resulted in similar particle sizes, around 3 nm on the different supports regardless of the Cu loading [49]. This allowed to study coalescence confined to the space of the cages and only dependent on the window size. Moreover, we changed the Cu loading in the narrow window m-MCF to study the effect of changing interparticle distance. Furthermore, we compared the stability of Cu catalysts supported by cage-like MCF and a non-cage-like SiO_2 support to investigate the influence of the support texture. The distribution and position of the Cu particles was determined using electron microscopy and tomography.

2. Experimental

2.1. MCF and m-MCF synthesis

Synthesis of both MCF (with large windows) and m-MCF (with small windows) was performed in 500 mL high-density polyethylene (HDPE) bottles. The bottles were filled with 150 mL 1.6 M HCl (130 mL demi-H_2O and 20 mL 37% HCl) and placed in a water bath at 30 °C. 4 g of P123, a triblock copolymer (Sigma-Aldrich) was added and the mixture was stirred overnight at 250 rpm to allow the polymer to dissolve. Trimethylbenzene (TMB, 98%, Sigma-Aldrich), which act as a swelling agent for the polymer, was added (4 g for MCF and 3 g for m-MCF) dropwise. After the addition, the temperature of the water bath was raised to 35 °C and the solution was stirred for 4 h. 9.2 mL of the SiO_2 precursor tetraethyl orthosilicate (TEOS, ≥ 99.0% Sigma-Aldrich) was added at once for MCF and 17 mL TEOS was added dropwise in 12 min with a syringe pump for m-MCF. 5 min after the addition of the TEOS the stirring bar was removed. The water bath was heated to 39 °C and the mixture was left at static conditions for 20 h. Only for the synthesis of MCF, 46 mg of NH_4F (p.a. ≥ 98%, Sigma-Aldrich) was added, while stirring. Subsequently, a hydrothermal treatment was performed for 24 h at 80 °C for MCF and at 70 °C m-MCF in a Heraeus muffle oven, under static conditions. Both MCF and m-MCF were washed by filtration with 4 L of demi-H_2O and dried at 60 °C. Next, the white powders were crushed and calcined at 550 °C for 6 h. The third support, a silica gel with pores of 3 nm (SG3), was obtained from Grace Davison. This type of silica gel generally contains impurities in the form of Fe_2O_3 (< 0.014%), Na_2O (< 0.15%), SO_4^{2-} (< 0.1%) and heavy metals (< $5{\cdot}10^{-4}$%) as provided by the manufacturer.

2.2. Catalyst synthesis

Typically, 1 g of SiO_2 support was dried at approximately 170 °C under dynamic vacuum for at least two hours to remove water from the pores. After the sample had cooled down to room temperature, the silica was impregnated with an aqueous $Cu(NO_3)_2$ (99% for analysis, Acros Organics) solution, acidified with 0.1 M HNO_3, using incipient wetness impregnation (IWI). The amount added was equal to the pore volume of the material and the concentration was adjusted to reach 2, 3 or 4 Cu atoms per nm^2 support surface area. The solid was mixed during and after the impregnation using a magnetic stirring bar. Subsequently the samples were dried under dynamic vacuum for 48 h. This relatively long drying period is required because of the large amount of sample, and it is known that thorough drying is essential to obtain uniform samples [35].

The impregnated and dried solids were loaded into a glass flow reactor and a heat treatment was performed in N_2 (350 °C, 1 h) [35,50] or 20% H_2 in N_2 (250 °C, 1.5 h) [49]. In both cases a heating rate of 2 °C/min was used. Samples with 2 Cu atoms/nm^2 were prepared on MCF and m-MCF using the N_2 treatment. Samples with 2 Cu atoms/nm^2 were prepared on SG3, MCF and m-MCF and with 3 or 4 Cu atoms/nm^2 on small window m-MCF, using the H_2 treatment. Only the five samples prepared using the H_2 treatment were selected for the stability tests in methanol synthesis and sieve fractions of 25–75 or 425-630 µm were made. Theses samples will be referred to as xCu_support, where the x is the number of Cu atoms/nm^2, being 2, 3 or 4 and the support being either SG3, MCF or m-MCF.

2.3. Characterization

N_2-physisorption was performed at −196 °C using a Micromeritics TriStar instrument. The samples were dried before the measurement under a N_2-flow at 300 °C, for at least 16 h. The total pore volume was determined at $p/p_0 = 0.995$. The pore size distributions were determined using the BJH method, assuming cylindrical pores.

The point of zero charge (PZC) of the support was determined by

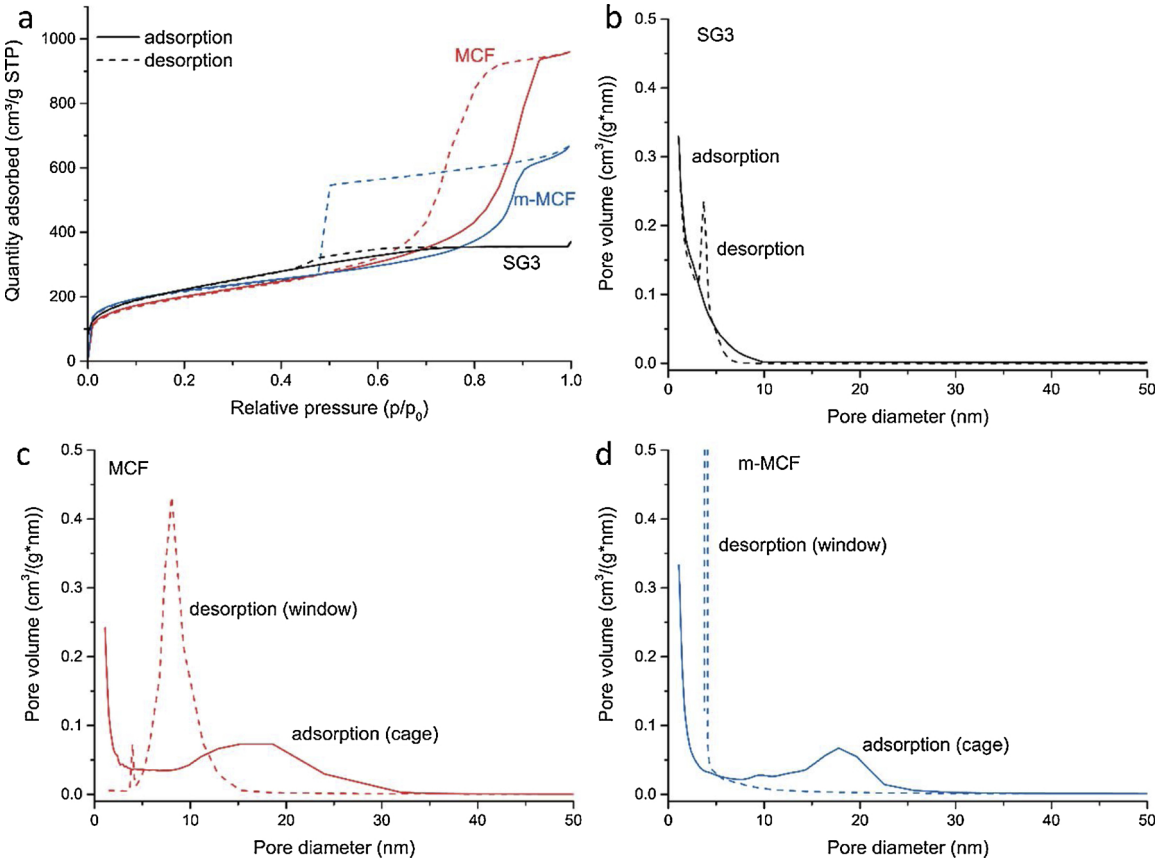

Fig. 1. a) N_2-physisorption isotherms of SG3, MCF and m-MCF. Pore size distributions of b) SG3, c) MCF and d) m-MCF. The solid lines are the pore size distributions obtained from the adsorption branches (indicating the cage sizes), and the dashed lines the distributions obtained from the desorption branches (indicating the window sizes). SG3 contains pores smaller than 5 nm. Both MCF and m-MCF display a cage size distribution of 10–25 nm, with an average of approximately 18 nm. MCF has an average window size of 8 nm and m-MCF has windows smaller than 3.8 nm.

adding small amounts of the support to a 10 mL solution of 0.1 M Ba $(NO_3)_2$. The pH of the solution was measured and SiO_2 was added until the pH stabilized. The pH at which the suspension stabilized was reported as the PZC [51–54].

X-ray diffraction (XRD) of the catalysts in oxidized state was performed using Bruker D2 phaser, using a 1.0 mm fixed slit. *In situ* XRD was performed using a Bruker D8 advance, equipped with a variable slit. Both machines were equipped with Co K_α radiation (λ = 1.78897 Å). An Anton-Paar XRK reaction chamber was filled for the *in situ* measurement with impregnated and dried m-MCF. A flow of 60 mL/min N_2 or 20% H_2 in N_2 was used. The cell was heated with 1 °C/min to 340 °C for the N_2 calcination and to 260 °C for the H_2 reduction, and the cell was kept at the highest temperature for 1 h. A diffractogram was recorded every 10 min. The crystallite sizes for the samples was determined using the Scherrer equation [55].

High-angle annular dark-field scanning transmission electron microscopy (HAADF-STEM) combined with energy dispersive X-ray (EDX) mapping was performed with a Talos™ F200X transmission electron microscope (FEI), operating at 200 keV. The MCF and m-MCF samples were embedded in a two-component epoxy resin (Epofix, EMS) and the resin was cured at 60 °C overnight. 70 nm thick slices were made with a Diatome 35° diamond knife mounted on a Reichert-Jung Ultracut E microtome. The slices were collected on a TEM grid. The samples supported by SG3 were ground and suspended in ethanol. After sonication the suspension was drop casted on a TEM grid. In both cases 300 mesh formvar Ni grids were. At least 200 particles were measured for each sample to determine the particle size distribution. Electron tomography was performed on 3Cu_m-MCF, before and after catalysis, to determine the location of the Cu nanoparticles in the SiO_2 support material. The slices were placed on a tomography grid (Quantifoil R2/1 carbon film supported parallel-bar Cu grid) and tilt series were obtained from -60 to 60° with steps of 4°. Alignment and reconstruction were performed with IMOD software.

2.4. Catalytic testing

The catalysts were tested in a two parallel reactor set-up of Autoclave Engineers under industrially relevant methanol synthesis conditions (40 bar and 270 °C). The relative high temperature (270 °C) was chosen to accelerate the nanoparticle mobility. 150–300 mg of catalyst was diluted with 1 mL SiC and loaded into the reactor. The catalyst bed was supported by a hollow steel tube and quartz wool to position the catalyst bed in the middle of the reactor. The Cu/SiO_2 samples were reduced *in situ* using a 110 mL/min flow of 20% H_2 in Ar at 250 °C A heating ramp of 2 °C/min was used and the reactor was kept at 250 °C for 2.5 h. After cooling down to 100 °C the gas mixture was switched to a premixed syngas mixture composed of 23% CO, 7% CO_2, 60% H_2 and 10% Ar. A carbonyl trap (heated to 50 °C), consisting of zeolite-Y and activated carbon, was placed before the reactor inlet to remove possible Fe- and/or Ni-carbonyls from the feed. The Ar acted as internal standard for the GC. After flushing for 30 min with the syngas mixture, the reactor was pressurized to 40 bar. All samples were tested using the same Cu-based weight hourly space velocity syngas (WHSV) of 16.5 $g_{syngas}/(g_{Cu}*h)$ to compare activity and stability. Three chromatograms were recorded before heating the reactor to determine the CO/Ar and CO_2/Ar ratio, and hence CO and CO_2 concentrations in the feed. Subsequently the reactor was heated to 270 °C with a heating rate of 2 °C/min. The products were analyzed by a Varian 450 on-line GC,

which was equipped with two columns. The first channel consisted of two series-connected HAYESEP Q (0.5Mx1/8") packed columns and a MOLSIEVE 13x (1.5Mx1/8") molecular sieve column connected to a TCD. This column was used to measure the CO/Ar and CO_2/Ar ratios during catalysis. By comparing the concentrations of CO and CO_2 in the off gas during catalysis with those in the original feed, the conversion of syngas and hence the activity of the catalyst was determined. Details of the activity and turn-over-frequency (TOF) calculation can be found in Equation S1-S10 in the SI. A channel consisting of a CP-SIL 8CB FS capillary column connected to an FID was used to detect the products (methanol, higher alcohols, dimethyl ether and alkanes). The selectivity was defined as the percentage of carbon atoms in the formed methanol divided by the total amount of carbon atoms in the products.

3. Results

3.1. Support characterization

The N_2-physisorption isotherms of SG3 (black), MCF (red) and m-MCF (blue) are displayed in Fig. 1a. The adsorption branch is related to the largest pores present and therefore indicates the size of the cages. The desorption branch is related to the small pores present in the material and therefore related to the size of the windows. The large hysteresis of both MCF and m-MCF, shows that in this case ink-bottle type pores are present [56]. The m-MCF shows a strong desorption at $p/p_0 = 0.48$ due to cavitation of N_2, indicating the presence of constrictions < 3.8 nm. For MCF the desorption takes place at higher pressures, indicating the presence of larger windows. This indicates that both MCF materials display a similar cage size, but a different window size [56].

The pore size distributions determined for SG3 (silica gel with 3 nm pores), MCF and m-MCF are shown in Fig. 1b–d, respectively. The size of the cages are displayed as solid lines in Fig. 1b–d and the size of the windows is indicated by the dashed lines. SG3 (frame b) displays pores with a diameter up to 10 nm, with the majority of the mesopores being 3 nm and therefore is referred to as SG3. MCF (frame c) and m-MCF (frame d) both show a broad cage size distribution, having an average size of 18 nm. The window size for MCF was 8 nm as determined from the desorption branch. The window size of m-MCF is smaller than 3.8 nm, however the exact size cannot be determined from the isotherm, because of the cavitation effect. The size of the window was reported before to be 2.3 nm for this preparation method [9].

Table 1 summarizes the BET surface area, the total pore volume, the micropore volume and the pore dimensions of the SiO_2 supports. The three materials display a similar surface area and the m-MCF displays a relative high micropore volume. The MCF materials have the same cage size, but a different window size. Also the PZC of the three supports is listed. The PZC of SG3 is 4.1, which is higher than those for the MCF (3.2) and m-MCF (3.5).

3.2. Cu deposition in mesocellular foam

As The m-MCF contains very narrow pores connecting the large cages hence a uniform deposition of Cu nanoparticles in the cages is challenging. The small windows limit the mobility of the $Cu(NO_3)_2$ during impregnation and drying. Therefore, we monitored the effect of the gas atmosphere during and after the formation of the Cu nanoparticles. *In situ* XRD and electron microscopy combined with energy dispersive X-ray (EDX) mapping were used to investigate the decomposition process and distribution of the Cu in a reducing (H_2) and inert (N_2) gas atmosphere.

For the preparation of Cu on different SiO_2 supports it has been shown that the use of N_2 flow during calcination leads to small (2 nm) Cu particles, uniformly distributed over the support, and the use of 2% NO in N_2 leads to larger (5–10 nm), clustered particles [35,50]. $Cu_2NO_3(OH)_3$ was suggested as immobile Cu-species during the calcination of $Cu(NO_3)_2$ in the presence of 2% NO, leading to the clusters [50]. The use of H_2 has been investigated to directly reduce the Cu $(NO_3)_2$ phase to Cu^0 [49], and to our knowledge *in situ* XRD has not

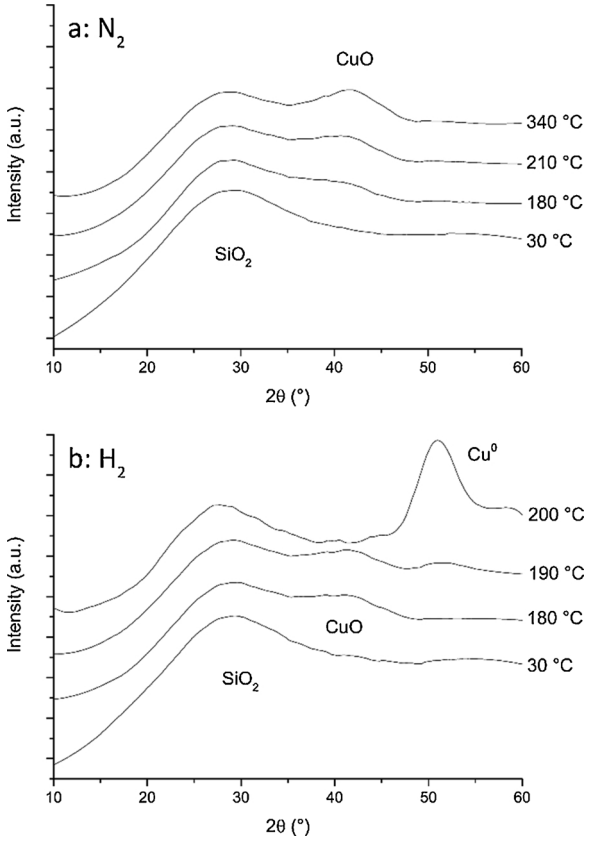

Fig. 2. *In situ* XRD of a) m-MCF (impregnated with $Cu(NO_3)_2$) during heating in N_2 and b) in 20% H_2 in N_2. The sample was heated with 1 °C/min and a total flow of 60 mL/min was used. In both cases the evolution of a peak at 41° 2ϑ, attributed to CuO, at 180 °C is observed. For the thermal treatment using H_2, this peak disappears simultaneously with the appearance of a diffraction line at 50.7° 2ϑ, attributed to crystalline Cu^0.

Table 1
Properties of the supports SG3, MCF and m-MCF. All three display a similar BET-surface area. SG3 has pores of 3 nm and the cage size of MCF and m-MCF is the same. The window size of MCF is 8 nm, much larger than the window size of m-MCF which is around 2.3 nm. The point of zero charge of SG3 was higher compared to the MCF supports.

	BET surface area (m^2/g)	Total pore volume[a] (cm^3/g)	Micropore volume (cm^3/g)	Cage size (nm)	Window size (nm)	PZC
SG3	805	0.56	0.03	3[b]	–	4.1
MCF	723	1.5	0.04	18	8	3.2
m-MCF	794	1.0	0.1	18	2.3[c]	3.5

[a] at $p/p_0 = 0.995$.
[b] average pore size.
[c] determined by Shakeri et al. [9].

been applied for the preparation of Cu/SiO_2 using H_2. Since the use of N_2 or H_2 are known to result in a uniform distribution of Cu on SiO_2 [35,50,57] and therefore the influence of these two procedures was tested for MCF and m-MCF.

Fig. 2 shows *in situ* XRD during heating in a N_2 (frame a) and 20% H_2 in N_2 (frame b) flow, of the small window m-MCF impregnated with an aqueous $Cu(NO_3)_2$ solution. The broad peak around 25° 2ϑ is due to the presence of amorphous SiO_2. In both frames a diffraction line is observed at 41° 2ϑ emerging around 180 °C, which is attributed to CuO. In N_2 (frame a) this peak narrows slightly with the temperature increasing to 340 °C, indicating growth of the CuO crystallites to a size of approximately 2 nm. In the presence of H_2 the CuO phase disappears between 190 and 200 °C, simultaneously with the appearance of a peak at 50.7° 2ϑ, showing the conversion of CuO to crystalline Cu^0.

The diffraction line of CuO after the N_2 reduction is less intense and has a lower area than the Cu^0 diffraction line after the H_2 treatment. This means that a significant part of the Cu-species after the N_2 treatment is X-ray invisible and hence CuO being in an amorphous state and therefore very likely highly dispersed on the SiO_2 surface. To determine the location of the Cu, energy dispersive X-ray (EDX) mapping in the electron microscope was performed. Fig. 3 shows the EDX maps of MCF particles prepared by heat treatment in N_2 (frame a) and in 20% H_2 in N_2 (frame b). The Cu signal is indicated in red and the Si signal in green. In both frames a and b, the Cu is distributed throughout the entire MCF particle. For the sample prepared in N_2 this is in agreement with Cu catalysts prepared on different SiO_2 structures by the same method [35,50]. The homogenous distribution of the Cu is in agreement with the observations from XRD shown in Fig. 2, that no crystalline $Cu_2NO_3(OH)_3$ was observed, which was before identified as an intermediate crystalline phase preventing mobility and redispersion of the Cu species over the SiO_2 support [50].

Fig. 3c shows a HAADF-STEM zoomed-in image of the edge of a MCF particle prepared by the N_2 treatment, together with the corresponding EDX maps of the area, showing the Cu (red), Si (green), combined Cu and Si, and the O (blue) signal. On the rim of the particle the Cu, as well as the Si (and O) signals are higher than at the inner area. The higher Si signal is likely due to the irregularity of the outer silica structure and implies a local high surface area of SiO_2. Bright features are clearly visible on the rim of the MCF particle, which indicates Cu particles. The absence of visible particles in the interior of

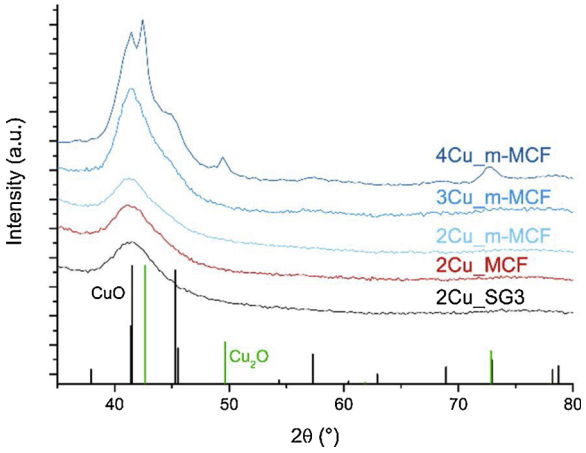

Fig. 4. X-ray diffractograms of the five samples prepared in H_2. The samples with 2 Cu atoms/nm^2 (2Cu_SG3 (black line), 2Cu_MCF (red line) and 2Cu_m-MCF (light blue line)) all have CuO crystallite sizes of 2.5 nm. 3Cu_m-MCF (medium blue) has a slightly larger crystallite size of 2.9 nm. The crystallite size of 4Cu_m-MCF (dark blue) was not determined as this sample is not purely CuO. However, from the narrow peaks it is be concluded that the crystallite size of this sample is larger than that of the other four samples (For interpretation of the references to colour in this figure legend, the reader is referred to the web version of this article).

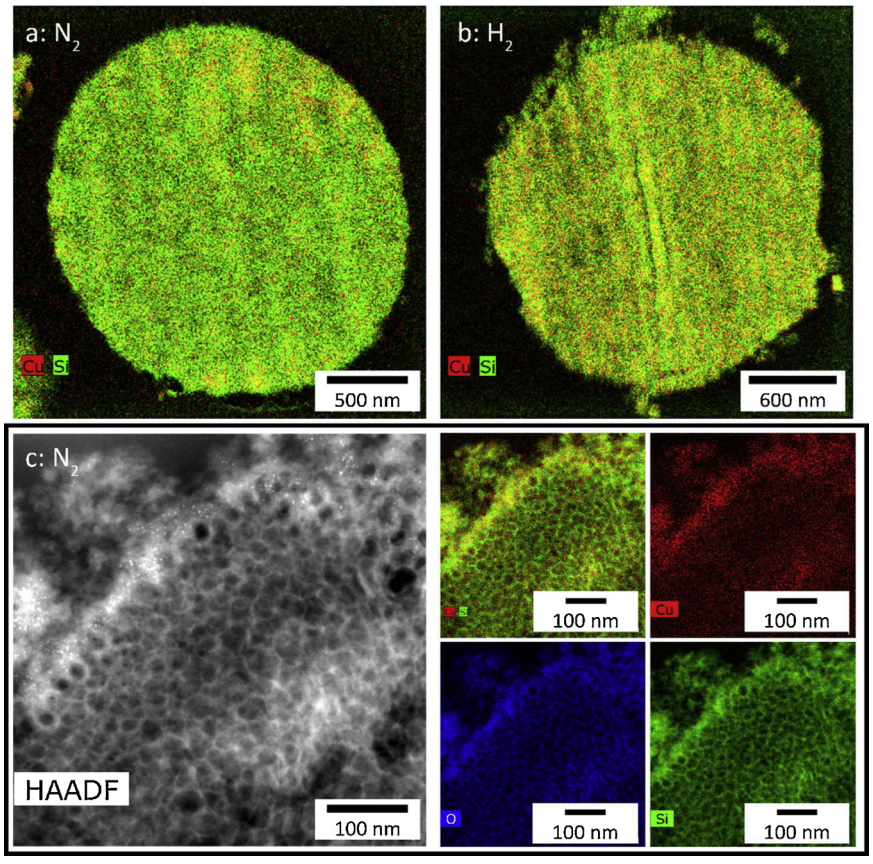

Fig. 3. EDX map of MCF particles containing Cu prepared by a) N_2 calcination and b) H_2 reduction. The EDX signal of Cu is indicated in red, the signal of Si in green. Both show a homogeneous distribution of Cu throughout the MCF particle. c) Zoom-in on the edge of a N_2 treated MCF particle, showing Cu particles in the HAADF-STEM image at the left, at the rim of the particle. In the interior of the MCF particle no Cu particles were observed, however Cu is present, meaning that this Cu is highly dispersed. The corresponing EDX maps of Cu (red), Si (green), the combined Cu and Si signal, and O (blue) are shown on the right of frame c. The Si signal at the edge of the particle is higher than in the interior. A higher Si signal is observed together with a higher Cu (and O) signal (For interpretation of the references to colour in this figure legend, the reader is referred to the web version of this article).

Table 2
Cu loadings of the five samples prepared in H_2 as the number of Cu atoms/nm^2 and the overall weight loading. Samples with 2 Cu atoms/nm^2 were synthesized on SG3, MCF and m-MCF, and with 3 and 4 Cu atoms/nm^2 on m-MCF. The samples containing 2 Cu atoms/nm^2 have the same crystallite size, as well as similar particle sizes determined from TEM images. The particle size and polydispersity for 3 and 4 Cu atoms/nm^2 on m-MCF increased slightly with the loading.

Sample	# Cu/nm^2	Cu weight loading (%)	d_{XRD} (nm)	d_N (TEM)[a] (nm)
2Cu_SG3	1.8	13.5	2.5	2.3 ± 07
2Cu_MCF	2.0	13.5	2.5	2.8 ± 0.8
2Cu_m-MCF	2.0	14.1	2.5	2.5 ± 0.7
3Cu_m-MCF	3.1	20.6	2.9	3.8 ± 2.4
4Cu_m-MCF	3.8	24.4	-[b]	4.3 ± 3.3

[a] calculated as $\frac{1}{N}\sum_{i=1}^{N} d_i$ b: Due to overlapping peaks and the presence of multiple phases in this samples the crystallite size was not determined.

the N_2 treated MCF indicates the presence of highly dispersed Cu-ions on the SiO_2 surface, because the Cu is located throughout the complete particle as observed from the EDX map.

From previous research it is known that very small particles or clusters are less active than larger particles in methanol synthesis. Using the decomposition of the $Cu(NO_3)_2$ phase in H_2 resulted in crystalline particles, which are visible in the interior of the MCF particles and are in the range of 2–4 nm. This means that the particles in the upper size range are larger than the windows of the m-MCF of approximately 2.3 nm. Hence, we chose to discuss here only the characteristics and catalytic performance of the H_2 treated samples, as they are excellently suited to study confinement of the Cu particles in the cages on the stability.

3.3. Influence of support and loading on Cu particle size

We investigated the influence of the Cu metal loading on the average particle size for the m-MCF support by varying the weight loading between 14 and 21%. In addition, we compared the particle size of Cu-particles prepared on SG3, MCF and m-MCF at a fixed metal loading. Fig. 4 displays X-ray diffractograms of the catalysts synthesized using H_2, prepared with various amounts of Cu and on the different supports. The number of Cu atoms per nm^2, the overall Cu loadings, the

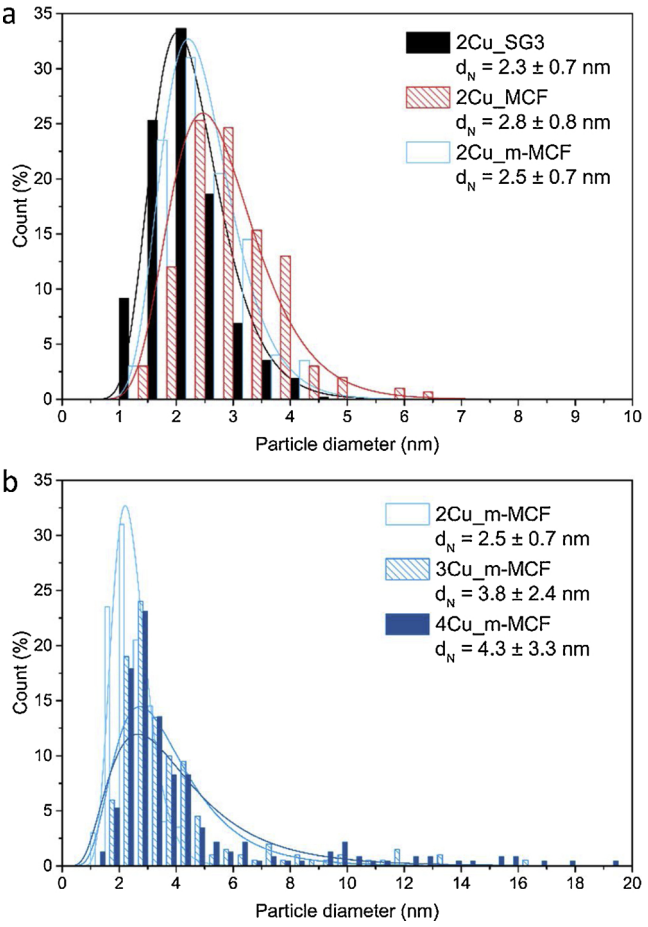

Fig. 6. Particle size distributions of a) the samples containing 2 Cu atoms/nm^2 2Cu_SG3, 2Cu_MCF and 2Cu_m-MCF) and b) the small window m-MCF supported samples with different loadings (2Cu_m-MCF, 3Cu_m-MCF and 4Cu_m-MCF). The samples containing 2 Cu atoms/nm^2 have similar particle sizes, in the range of 2–5 nm. The samples with the higher loadings in frame b display a larger particle size (up to 20 nm) and with increasing size the polydispersity increases. The lines represent a lognormal distribution.

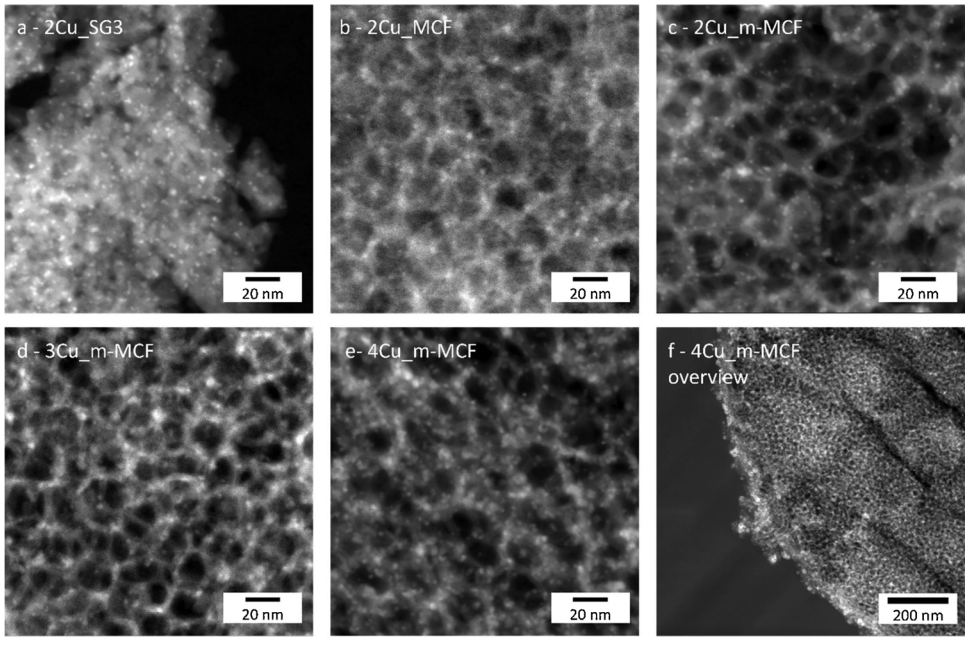

Fig. 5. STEM images of a) 2Cu_SG3, b) 2Cu_MCF, c) 2Cu_m-MCF, d) 3Cu_m-MCF and e) and f) 4Cu_m-MCF. For all samples the Cu is evenly distributed over the support and similar particles sizes were observed. Frame f shows an overview of 4Cu_m-MCF, showing a higher concentration of Cu, and larger Cu particles at the outside of the MCF particle. This shows that for the samples with a higher loading the particle size distribution is larger.

Table 3
Conversion of CO + CO_2 (%), the Cu based methanol yield ($mol_{MeOH}/(g_{Cu}*s)$), the methanol selectivity (%, carbon-atom based) and the surface averaged particle size (nm) and turn-over-frequency (s^{-1}) at the start and end of the catalytic run. The selectivity towards methanol increases with increasing conversion and the TOF increases with increasing particle size.

	X_{CO+CO2}, t = 0 (%)	Cu-based MeOH yield ($*10^{-6}$ $mol_{MeOH}/(g_{Cu}*s)$), t = 0	MeOH selectivity (%)	d_S[a] (nm) (σ (nm)), t = 0	TOF, t = 0 ($*10^{-3}$ s^{-1})	d_S[a] (nm) (σ (nm)), t = 300 h	TOF, t = 300 h ($*10^{-3}$ s^{-1})
2Cu_SG3	6.3	5.9	94.2	2.4 ± 0.7	0.91	4.8 ± 1.7	1.11
2Cu_MCF	10.7	10	97.0	2.9 ± 0.9	1.76	4.7 ± 1.4	2.27
2Cu_m-MCF	6.4	5.5	95.3	2.5 ± 0.7	0.88	4.2 ± 1.6	1.14
3Cu_m-MCF	6.4	5.5	92.0	4.5 ± 2.4	1.58	5.3 ± 2.5	1.34
4Cu_m-MCF	7.9	7.7	95.7	5.4 ± 3.5	2.25	7.2 ± 3.7	2.18

[a] calculated as $\sqrt{\frac{1}{N}\sum_{i=1}^{N} d_i^2}$.

crystallite sizes and the number averaged particle sizes (d_N) are given in Table 2. The broad diffraction line around 41° 2ϑ, visible in all patterns in Fig. 4, is due to the presence of small CuO crystallites. 4Cu_m-MCF shows additional diffraction lines at 42.6 and 49.6° 2ϑ which are ascribed to the presence of crystalline Cu_2O. The crystallite sizes of all samples containing 2 Cu atoms/nm^2, supported on SG3, MCF and m-MCF, were very similar; 2.5 nm. With increasing loading the crystallite sizes increase to 2.9 nm for sample 3Cu_m-MCF (3 Cu atoms/nm^2 on m-MCF). Only 4Cu_m-MCF (4 Cu atoms/nm^2 on m-MCF) shows additionally narrow peaks, which is an indication that this sample contains also large CuO crystallites.

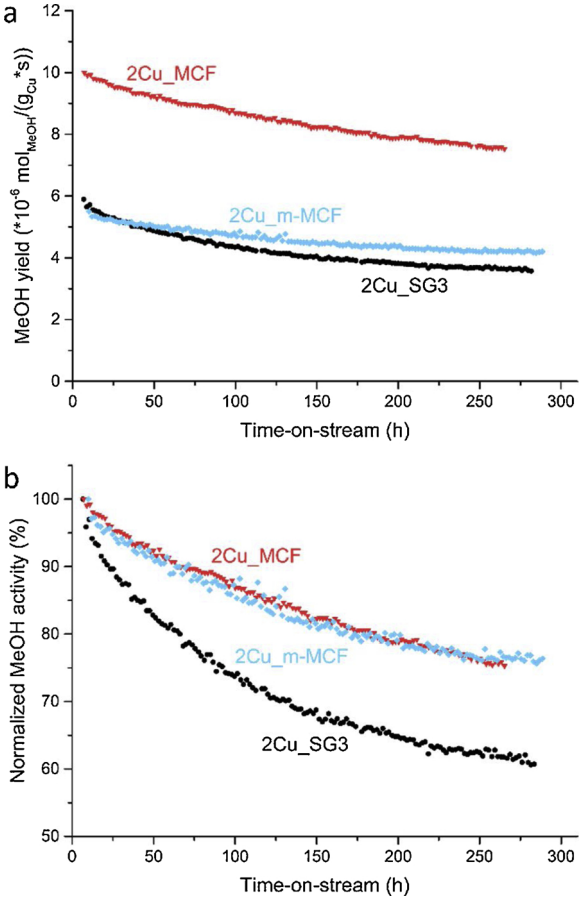

Fig. 7. a) methanol yield per second, per gram of Cu and b) the normalized MeOH yield for the catalysts containing 2 Cu atoms/nm^2 supported on SG3 (black circles), MCF (red down triangles) and m-MCF (light blue diamonds). The activity was measured at 40 bar syngas (23% CO, 7% CO_2, 60% H_2 and 10% Ar) and 270 °C. 2Cu_SG3 and 2Cu_m-MCF display a lower activity than 2Cu_MCF due to embedment of the particles in the narrow pores. The catalysts supported by MCF and m-MCF have a higher stability compared to 2Cu_SG3, likely because of the concave surface of the cage-like MCF (For interpretation of the references to colour in this figure legend, the reader is referred to the web version of this article).

Fig. 5 shows representative HAADF-STEM images of 2Cu_SG3 (frame a), 2Cu_MCF (frame b), 2Cu_m-MCF (frame c), 3Cu_m-MCF (frame d) and 4Cu_m-MCF (frame e and f). In all three cases the nanoparticles are uniformly distributed over the support. The cage diameters (frames b–f) were around 20 nm, in agreement with the size determined from N_2-physisorption. All samples contain small particles of 2.5–3.0 nm. Fig. 5f shows an overview image of 4Cu_m-MCF and shows a few larger particles at the outside of the m-MCF particle. This was also observed, although to a lesser extent, for 3Cu_m-MCF.

Fig. 6a shows the particle size distribution for the samples containing 2 Cu atoms/nm^2 and Fig. 6b shows the particle size distributions for the samples supported by m-MCF. For the samples containing 2 Cu atoms/nm^2 the particle sizes and polydispersity were very similar on the different supports (2.3–2.8 nm ± 0.7-0.8 nm). For the m-MCF supported samples the size and polydispersity increased with increasing loading (2.5 ± 0.7 nm for 2Cu_m-MCF, 3.8 ± 2.4 nm for 3Cu_m-MCF and for 4.3 ± 3.3 nm 4Cu_m-MCF). These results are in line with the values obtained from XRD and expectations based on literature [49].

This method of impregnation and reduction in H_2 allows to create similar particle size on different supports (SG3, MCF and m-MCF) and on m-MCF with different metal loadings, ranging from 2 to 4 Cu atoms/nm^2. Having the same particle size for the different samples makes it possible to compare the stability of these catalysts on the different supports and study the effect of interparticle distance.

3.4. Influence of support on catalyst activity and stability

Table 3 lists CO + CO_2 conversion (in %), the Cu-based methanol yield (in $mol_{MeOH}/(g_{Cu}*s)$), the methanol selectivity (in %, carbon atom based) and the surface averaged particle size, determined by TEM before and after catalysis. Also the turn-over-frequency (TOF) at the start and end of the catalytic run (in s^{-1}) is listed in Table 3. Figure S1 plots the dependency of the TOF on the particle diameter. Representative images of the spent catalysts are shown in Figure S2 and corresponding particle size distributions comparing the fresh and spent samples in Figure S3. Methanol was in all cases the dominant product, with selectivities being 92% and above. The side products mainly consisted of methane and dimethyl ether. The TOF increases slightly with increasing particle size as shown before for Cu catalysts in methanol synthesis [48]. The TOF for our samples were slightly higher than determined by Van den Berg et al. which is explained by the fact that the activity in this paper was measured at 270 °C instead of 260 °C in reference [48].

We first discuss the influence of the type of support on the catalyst activity. The Cu-based methanol yields (in $mol_{MeOH}/(g_{Cu}*s)$) versus time-on-stream are shown for the samples containing 2 Cu atoms/nm^2 in Fig. 7a. The initial methanol yields are lower for 2Cu_SG3 and

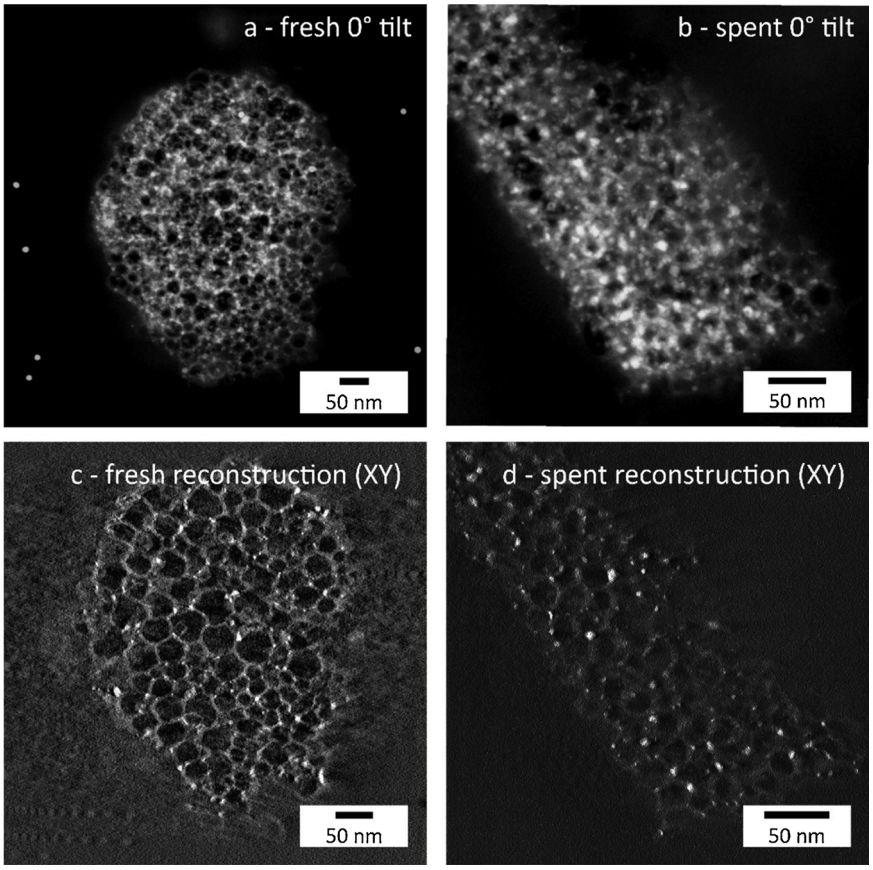

Fig. 8. STEM images at 0° tilt are shown in a) for the fresh catalyst and b) for the spent catalyst 3Cu_m-MCF. The reconstructed images, c) fresh and d) spent, reveal nanoparticles located inside the cages of the m-MCF support. However, some particles seem to be located in the small connecting windows of the m-MCF.

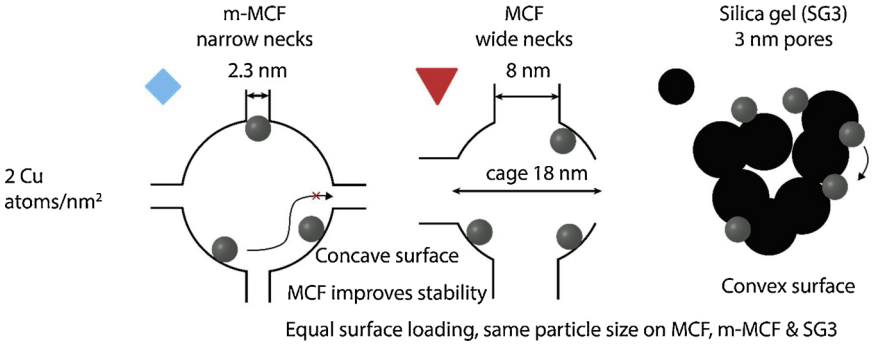

Fig. 9. Schematic representation of the catalysts containing 2 Cu atoms/nm^2 on the different supports. The MCF supported catalysts display a higher stability compared to the one supported by SG3. The colored shapes at the left upper corner of the representation of each sample indicate the symbols used to present the catalytic data in Fig. 7. The Cu particle size on the different supports were very similar, and the use of MCF improved the stability of the catalysts during methanol synthesis, likely due to the concave surface of MCF. The difference in stability between the narrow window m-MCF and large window MCF was small, although the slightly higher stability of the m-MCF supported catalyst might be attributed to the small entrances.

2Cu_m-MCF than for 2Cu_MCF and the related differences in TOF persist, also upon prolonged catalysis. As the particle sizes and distributions are very similar, and the loadings as well, the only other factor that can explain different activities is the texture of the supports. The contact between the support and the metal nanoparticles can influence the active metal surface area. Hence these differences are tentatively explained by confinement of the Cu particles in the small pores of SG3 and the micropores of m-MCF, and thereby blocking part of the Cu surface area (up to almost half) by silica, making it inaccessible for the catalytic reaction.

To investigate this effect of embedding in more detail, electron tomography was performed, because from a 2D (transmission) image the location of the particles in the support cannot be determined. Electron tomography was performed on the sample with 3 Cu atoms/nm^2 supported on m-MCF prior to and after catalysis. Fig. 8a and b show the 0° tilt HAADF-STEM image of a fresh and spent particle of 3Cu_m-MCF, respectively. Fig. 8c and d show the reconstructed image of the XY plane of a fresh and spent catalyst particle, respectively. The full tilt series and corresponding reconstruction of the fresh and spent catalyst can be found in the SI, M1 and M2, respectively.

From the reconstructed XY-view it can be seen that part of the Cu particles are located in the cages and part of the particles are located at/in the walls or connecting windows of the m-MCF support. The surface of the nanoparticles located in the windows of the small window MCF is likely not fully accessible for the syngas and therefore does not fully participate in the catalytic reaction. This can explain the lower activity of the m-MCF and SG3 supported catalysts compared to the large window MCF supported catalysts. In addition, the particles of the spent sample in Fig. 8b and d are slightly larger and therefore the location is more clear. Some particles could be in the windows, however the majority seems to be located in the cages of the m-MCF.

Fig. 7b compares the stability based on the normalized activity of the samples containing 2 Cu atoms/nm^2 on the different supports. The first major difference is that the two MCF samples display a much

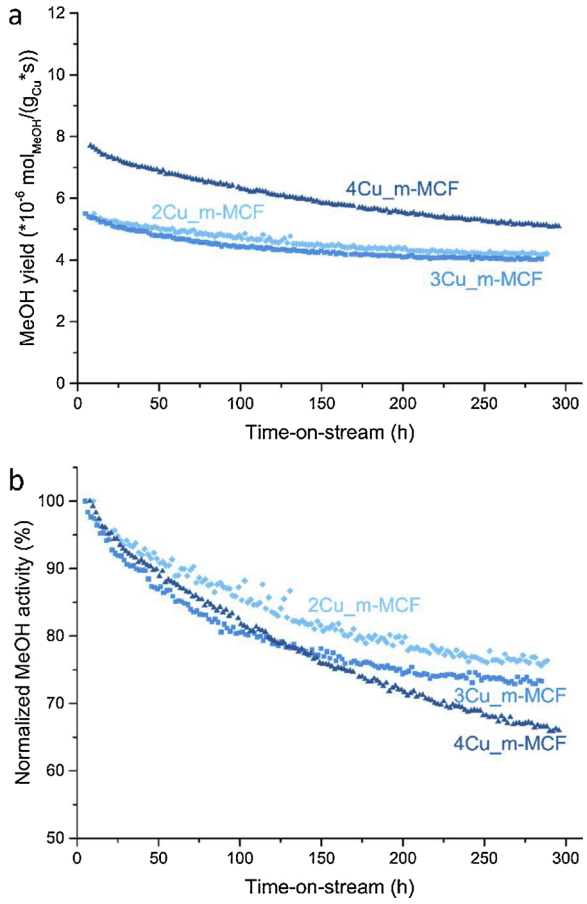

Fig. 10. a) methanol yield per second, per gram of Cu and b) the normalized MeOH yield for the catalysts supported by the narrow window m-MCF with different weight loadings: 2Cu_m-MCF (light blue diamonds), 3Cu_m-MCF (medium blue squares), and 4Cu_m-MCF (dark blue up triangles). The activity was measured at 40 bar syngas (23% CO, 7% CO_2, 60% H_2 and 10% Ar) and 270 °C. The activity of 4Cu_m-MCF is higher compared to the samples with the lower loadings, because the particles are larger and therefore display a higher TOF. Moreover, the majority of the particles in 4Cu_m-MCF are larger than the window size and embedding is likely to be less. 2Cu_m-MCF displays the highest stability. The initial stability of 3Cu_m-MCF is lower due to a smaller interparticle distance and therefore a higher rate of coalescence. The polydispersity of the Cu particles in 4Cu_m-MCF is the highest and therefore displays the highest Ostwald ripening rate (For interpretation of the references to colour in this figure legend, the reader is referred to the web version of this article).

higher stability than the SG3 sample; the MCF samples lose approximately 20% of their initial activity, where the SG3 supported catalysts loses 40%. Impurities such as Na and S in the SG3 might influence the catalyst activity. However, as the silica support is relatively pure and as we do not see a difference in activity between 2Cu_SG3 and 2Cu_m-MCF, it is unlikely that impurities have a large influence on the catalyst performance. The largest difference in deactivation is observed in the first 100 h. The deactivation caused by coalescence is expected at short time scales, since coalescence will minimize as the particles reach a larger size and larger interparticle distance. Ostwald ripening is expected to be a continuous process. As the polydispersity in the samples is the same, we do not expect large differences in the Ostwald ripening contribution. Hence the different stabilities are likely caused by different coalescence rates.

Fig. 9 schematically represents the textures of the different supports. The difference in rate of coalescence might be explained by the different support textures, with particles being more stable on a concave surface of MCF compared to the convex surface of the silica gel. An additional factor that might explain the influence of the type of silica support as observed in Fig. 7b might be the difference in point of zero charge (PZC) of the silicas. The SG3 displays a higher PZC (4.1) compared to the more acidic MCF (PZC = 3.2) and m-MCF (PZC = 3.5). A higher stability of MCF supported Au catalysts compared to silica gel supported Au was observed before for the liquid phase oxidation of 5-hydroxymethyl furfural [16].

The difference in stability between 2Cu_MCF and 2Cu_m-MCF is small, but significant. The deactivation of 2Cu_m-MCF is slightly faster in the first 200 h. After 250 h time-on-stream the two curves cross and the m-MCF is more stable than the MCF supported catalyst. Although the difference is small this might be attributed to the smaller window size of m-MCF. Particle growth on long time scales in m-MCF is likely reduced when the Cu particles reach a size larger than the window size. However, the differences are not very large within our experimental time scale, and longer experiments would be useful to proof this point with more certainty.

3.5. Influence of Cu loading on catalyst activity and stability

As described in the previous section the support type has a major influence on the catalysts stability. To disentangle the parameters affecting the stability even further we varied the Cu loading on the narrow window m-MCF. The Cu-based methanol yields (in $mol_{MeOH}/(g_{Cu}*s)$) versus time-on-stream are shown for the narrow windowed m-MCF supported catalysts with different catalyst loadings in Fig. 10a. 4Cu_m-MCF contains larger particles than 3Cu_m-MCF, which again contains somewhat larger particles than 2Cu_m-MCF, which explains the higher activity and TOF with increasing loadings, as it is known that larger Cu particles have a higher TOF [48].

Fig. 10b shows the stability of the m-MCF supported catalyst with the different loadings of 2, 3 and 4 Cu atoms/nm^2. The long-term stability decreases with higher Cu loadings. Particle growth results on one side to loss in surface area and on the other to an increase in TOF. The loss in activity for 2Cu_m-MCF and 3Cu_m-MCF is not very different after 270 h, but the shape of the curves is clearly different. The initial deactivation of 3Cu_m-MCF is much faster compared to 2Cu_m-MCF. This is likely due to the smaller interparticle distance in 3Cu_m-MCF and therefore faster coalescence. 2Cu_m-MCF and 3Cu_m-MCF show both a high stability and almost no deactivation after 270 h time-on-stream.

4Cu_m-MCF displays the lowest stability of the m-MCF supported samples and is not yet stable after 300 h of methanol synthesis. Although the initial deactivation rate is lower than for 3Cu_m-MCF, the catalyst continuously deactivates. The ongoing deactivation of this sample strongly suggest that Ostwald ripening is the predominant particle growth mechanism. This is in agreement with the fact that the larger particles in 4Cu_m-MCF make particle coalescence less likely while the high polydispersity in particle size favors Ostwald ripening, as discussed before. Furthermore, for samples like 2Cu_m-MCF, with a suboptimal Cu particle size, the loss in activity is somewhat mitigated by an increase in TOF upon particle growth, this effect becomes less important for 4Cu_m-MCF, where the Cu particles had a significantly larger initial particle size.

4. Conclusion

MCF (with large windows) and modified-MCF (with small windows) were synthesized, having both the same specific surface area and cage size. A homogeneous distribution of Cu particles was obtained by calcination in N_2 and by direct reduction in H_2 of the impregnated Cu $(NO_3)_2$ phase. However, calcination in N_2 led to highly dispersed Cu being less suitable for methanol synthesis than the 3 nm Cu particles obtained by using H_2. Samples with the same Cu loading were prepared on MCF, m-MCF as well as on a silica gel with 3 nm pores. Using MCF and m-MCF as support for Cu/SiO_2 catalysts improved the stability dramatically compared to using SG3 (silica gel with 3 nm pores) while

the window size of MCF had little impact. Furthermore samples with a higher Cu loading on m-MCF were prepared, which led to a larger Cu particle size and larger polydispersity in size. Electron tomography revealed that part of the Cu nanoparticles was located inside the cages and some of the particles were likely located in the windows. Using a loading of 3 Cu atoms/nm^2 on m-MCF exposed a high stability during methanol synthesis after approximately 200 h. In this case the particle diameter exceeded the window size and particles were trapped in the cages of the SiO_2. A smaller interparticle distance resulted in a higher rate of coalescence and a higher polydispersity to a higher rate of Ostwald ripening during catalysis. The incipient wetness impregnation of $Cu(NO_3)_2$, followed by direct reduction in H_2 allows the entrapment of Cu nanoparticles inside mesoporous SiO_2, generating a highly stable methanol synthesis catalyst.

Acknowledgements

Marjan Versluijs-Helder and Dennie Wezendonk are thanked for performing the *in situ* XRD measurements and Jan Willem de Rijk for maintenance of the high-pressure methanol synthesis reactor. Christa van Oversteeg is acknowledged for measuring the point-of-zero charge of the silica supports and Remco Dalebout for performing the N_2-physisorption measurements and analysis. Grace Davison is thanked for providing the silica gel. This project was funded by NWO Vici project no. 16.130.344 and the European Research Council, project number ERC-2014-CoG 648991.

Appendix A. Supplementary data

Supplementary data associated with this article can be found, in the online version, at https://doi.org/10.1016/j.cattod.2019.01.053.

References

[1] S.B. McCullen, J.C. Vartuli, Method for stabilizing synthetic mesoporous crystalline material, US 5156829, (1998) doi:US005485919A.
[2] C.T. Kresge, M.E. Leonowicz, W.J. Roth, J.C. Vartuli, J.S. Beck, Ordered mesoporous molecular sieves synthesized by a liquid-crystal template mechanism, Nature 359 (1992) 710–712, https://doi.org/10.1038/359710a0.
[3] J.S. Beck, J.C. Vartuli, W.J. Roth, M.E. Leonowicz, C.T. Kresge, K.D. Schmitt, C.T.W. Chu, D.H. Olson, E.W. Sheppard, S.B. McCullen, J.B. Higgins, J.L. Schlenker, A new family of mesoporous molecular sieves prepared with liquid crystal templates, J. Am. Chem. Soc. 114 (1992) 10834–10843, https://doi.org/10.1021/ja00053a020.
[4] D. Zhao, J. Feng, Q. Huo, N. Melosh, G.H. Fredrickson, B.F. Chmelka, G.D. Stucky, Triblock copolymer syntheses of Mesoporous Silica with periodic 50 to 300 angstrom pores, Science 279 (1998) 548–552, https://doi.org/10.1126/science.279.5350.548.
[5] D. Zhao, Q. Huo, J. Feng, B.F. Chmelka, G.D. Stucky, Tri-, Tetra-, and octablock copolymer and nonionic surfactant syntheses of highly ordered, hydrothermally stable, mesoporous silica structures, J. Am. Chem. Soc. 120 (1998) 6024–6036, https://doi.org/10.1021/Ja974025i.
[6] P. Schmidt-Winkel, W.W. Lukens Jr, D. Zhao, P. Yang, B.F. Chmelka, G.D. Stucky, Mesocellular siliceous foams with uniformly sized cells and windows, J. Am. Chem. Soc. 121 (1999) 254–255, https://doi.org/10.1021/ja983218i.
[7] P. Schmidt-Winkel, W.W. Lukens Jr, P. Yang, D.I. Margolese, J.S. Lettow, J.Y. Ying, G.D. Stucky, Microemulsion templating of siliceous mesostructured cellular foams with well-defined ultralarge mesopores, Chem. Mater. 12 (2000) 686–696, https://doi.org/10.1021/cm991097v.
[8] Y. Han, S.S. Lee, J.Y. Ying, Pressure-driven enzyme entrapment in siliceous mesocellular foam, Chem. Mater. 18 (2006) 643–649, https://doi.org/10.1021/cm0520618.
[9] M. Shakeri, L. Roiban, V. Yazerski, G. Prieto, R.J.M. Klein Gebbink, P.E. de Jongh, K.P. de Jong, Engineering and sizing nanoreactors to confine metal complexes for enhanced catalytic performance, ACS Catal. 4 (2014) 3791–3796, https://doi.org/10.1021/cs500777q.
[10] W. Li, P. Bollini, S.A. Didas, S. Choi, J.H. Drese, C.W. Jones, Structural changes of silica mesocellular foam supported amine-functionalized CO2 adsorbents upon exposure to steam, ACS Appl. Mater. Interfaces 2 (2010) 3363–3372, https://doi.org/10.1021/am100786z.
[11] C. Li, Chiral synthesis on catalysts immobilized in Microporous and mesoporous materials, Catal. Rev. Sci. Eng. 46 (2004) 419–492, https://doi.org/10.1081/CR-200036734.
[12] Z. Huang, W. Pan, H. Zhou, F. Qin, H. Xu, W. Shen, Nafion-resin-modified mesocellular silica foam catalyst for 5-hydroxymethylfurfural production from D-fructose, ChemSusChem 6 (2013) 1063–1069, https://doi.org/10.1002/cssc.201200967.
[13] W.T. Ralston, G. Melaet, T. Saephan, G.A. Somorjai, Evidence of structure sensitivity in the Fischer–Tropsch reaction on model cobalt nanoparticles by time-resolved chemical transient kinetics, Angew. Chemie - Int. Ed. 56 (2017) 7415–7419, https://doi.org/10.1002/anie.201701186.
[14] N. Musselwhite, K. Na, S. Alayoglu, G.A. Somorjai, The pathway to total isomer selectivity: n-Hexane Conversion (Reforming) on platinum nanoparticles supported on aluminum modified mesoporous silica (MCF-17), J. Am. Chem. Soc. 136 (2014) 16661–16665, https://doi.org/10.1021/ja509638w.
[15] G. Wang, R. van den Berg, C. de Mello Donega, K.P. de Jong, P.E. de Jongh, Silica-supported Cu_2O nanoparticles with tunable size for sustainable hydrogen generation, Appl. Catal. B Environ. 192 (2016) 199–207, https://doi.org/10.1016/j.apcatb.2016.03.044.
[16] N. Masoud, B. Donoeva, P.E. de Jongh, Stability of gold nanocatalysts supported on mesoporous silica for the oxidation of 5-hydroxymethyl furfural to furan-2,5-dicarboxylic acid, Appl. Catal. A Gen. 561 (2018) 150–157, https://doi.org/10.1016/j.apcata.2018.05.027.
[17] R.N. Widyaningrum, T.L. Church, M. Zhao, A.T. Harris, Mesocellular-foam-silica-supported Ni catalyst: effect of pore size on H_2 production from cellulose pyrolysis, Int. J. Hydrogen Energy 37 (2012) 9590–9601, https://doi.org/10.1016/j.ijhydene.2012.03.052.
[18] S.S. Lee, S.N. Riduan, N. Erathodiyil, J. Lim, J.L. Cheong, J. Cha, Y. Han, J.Y. Ying, Magnetic nanoparticles entrapped in siliceous mesocellular foam: a new catalyst support, Chem. - A Eur. J. 18 (2012) 7394–7403, https://doi.org/10.1002/chem.201102361.
[19] E.W. Ping, R. Wallace, J. Pierson, T.F. Fuller, C.W. Jones, Highly dispersed palladium nanoparticles on ultra-porous silica mesocellular foam for the catalytic decarboxylation of stearic acid, Microporous Mesoporous Mater. 132 (2010) 174–180, https://doi.org/10.1016/j.micromeso.2010.02.017.
[20] M. Shakeri, C.W. Tai, E. Göthelid, S. Oscarsson, J.E. Bäckvall, Small Pd nanoparticles supported in large pores of mesocellular foam: an excellent catalyst for racemization of amines, Chem. - A Eur. J. 17 (2011) 13269–13273, https://doi.org/10.1002/chem.201101265.
[21] E.V. Johnston, O. Verho, M.D. Kärkäs, M. Shakeri, C.W. Tai, P. Palmgren, K. Eriksson, S. Oscarsson, J.E. Bäckvall, Highly dispersed palladium nanoparticles on mesocellular foam: an efficient and recyclable heterogeneous catalyst for alcohol oxidation, Chem. - A Eur. J. 18 (2012) 12202–12206, https://doi.org/10.1002/chem.201202157.
[22] C. Na-Chiangmai, N. Tiengchad, P. Kittisakmontree, O. Mekasuwandumrong, J. Powell, J. Panpranot, Characteristics and catalytic properties of mesocellular foam silica supported Pd nanoparticles in the liquid-phase selective hydrogenation of phenylacetylene, Catal. Lett. 141 (2011) 1149–1155, https://doi.org/10.1007/s10562-011-0593-3.
[23] O. Verho, A. Nagendiran, E.V. Johnston, C.W. Tai, J.E. Bäckvall, Nanopalladium on amino-functionalized mesocellular foam: an efficient catalyst for suzuki reactions and transfer hydrogenations, ChemCatChem 5 (2013) 612–618, https://doi.org/10.1002/cctc.201200247.
[24] S. Guo, J. Wang, C. Ding, Q. Duan, Q. Ma, K. Zhang, P. Liu, Confining Ni nanoparticles in honeycomb-like silica for coking and sintering resistant partial oxidation of methane, Int. J. Hydrogen Energy 43 (2018) 6603–6613, https://doi.org/10.1016/j.ijhydene.2018.02.035.
[25] J. Sun, D. Ma, H. Zhang, X. Liu, X. Han, X. Bao, G. Weinberg, N. Pfa, Toward Monodispersed Silver Nanoparticles with Unusual Thermal Stability, (2006), pp. 15756–15764, https://doi.org/10.1021/ja064884j.
[26] J. Richardson, J. Propp, Pore size effects on sintering of Ni/Al_2O_3 catalysts, J. Catal. 467 (1986) 457–467, https://doi.org/10.1016/0021-9517(86)90333-7.
[27] E. Ruckenstein, B. Pulvermacher, Effect of the pore size on the aging of supported metals, J. Catal. 37 (1975) 416–423, https://doi.org/10.1016/0021-9517(75)90178-5.
[28] M.T. Bore, H.N. Pham, E.E. Switzer, T.L. Ward, A. Fukuoka, A.K. Datye, The role of pore size and structure on the thermal stability of gold nanoparticles within mesoporous silica, J. Phys. Chem. B 109 (2005) 2873–2880, https://doi.org/10.1021/jp045917p.
[29] V.F. Puntes, I. Kiricsi, J. Zhu, J.W. Ager, M.K. Ko, H. Frei, P. Alivisatos, G.A. Somorjai, Synthetic insertion of gold nanoparticles into mesoporous silica, Chem. Mater. 15 (2003) 1242–1248, https://doi.org/10.1021/cm020824a.
[30] L. de Rogatis, M. Cargnello, V. Gombac, B. Lorenzut, T. Montini, P. Fornasiero, Embedded phases: a way to active and stable catalysts, ChemSusChem 3 (2010) 24–42, https://doi.org/10.1002/cssc.200900151.
[31] G. Prieto, H. Tüysüz, N. Duyckaerts, J. Knossalla, G.-H. Wang, F. Schüth, Hollow nano- and microstructures as catalysts, Chem. Rev. 116 (2016) 14056–14119, https://doi.org/10.1021/acs.chemrev.6b00374.
[32] P.M. Arnal, M. Comotti, F. Schüth, High-temperature-stable catalysts by hollow sphere encapsulation, Angew. Chem. 118 (2006) 8404–8407, https://doi.org/10.1002/ange.200603507.
[33] G. Prieto, J.D. Meeldijk, K.P. de Jong, P.E. de Jongh, Interplay between pore size and nanoparticle spatial distribution: consequences for the stability of $CuZn/SiO_2$ methanol synthesis catalysts, J. Catal. 303 (2013) 31–40, https://doi.org/10.1016/j.jcat.2013.02.023.
[34] G. Prieto, M. Shakeri, K.P. de Jong, P.E. de Jongh, Quantitative relationship between support porosity and the stability of pore-confined metal nanoparticles studied on $CuZn/SiO_2$ methanol synthesis catalysts, ACS Nano 8 (2014) 2522–2531, https://doi.org/10.1021/nn406119j.
[35] G. Prieto, J. Zečević, H. Friedrich, K.P. de Jong, P.E. de Jongh, Towards stable catalysts by controlling collective properties of supported metal nanoparticles, Nat.

Mater. 12 (2013) 34–39, https://doi.org/10.1038/nmat3471.
[36] I.M. Lifshitz, V.V. Slyozov, The kinetics of precipitation from supersaturated solid solutions, J. Phys. Chem. Solids 19 (1961) 35–50, https://doi.org/10.1016/0022-3697(61)90054-3.
[37] P. Wynblatt, N.A. Gjostein, Supported metal crystallites, Prog. Solid State Chem. 9 (1975) 21–58, https://doi.org/10.1016/0079-6786(75)90013-8.
[38] P.J.F. Harris, Growth and structure of supported metal catalyst particles, Int. Mater. Rev. 40 (1995) 97–115, https://doi.org/10.1179/095066095790326102.
[39] K.C. Waugh, Methanol synthesis, Catal. Today 15 (1992) 51–75, https://doi.org/10.1016/0920-5861(92)80122-4.
[40] R. Malhotra, Fossil Energy: Selected Entries from the Encyclopedia of Sustainability Science and Technology, Springer New York, New York, NY, 2013, https://doi.org/10.1007/978-1-4614-5722-0_1.
[41] H.H. Kung, Deactivation of methanol synthesis catalysts - a review, Catal. Today 11 (1992) 443–453, https://doi.org/10.1016/0920-5861(92)80037-N.
[42] S. Kuld, M. Thorhauge, H. Falsig, C.F. Elkjær, S. Helveg, I. Chorkendorff, J. Sehested, Quantifying the promotion of Cu catalysts by ZnO for methanol synthesis, Science. 352 (2016) 969–974, https://doi.org/10.1126/science.aaf0718.
[43] M.B. Fichtl, D. Schlereth, N. Jacobsen, I. Kasatkin, J. Schumann, M. Behrens, R. Schlögl, O. Hinrichsen, Kinetics of deactivation on $Cu/ZnO/Al_2O_3$ methanol synthesis catalysts, Appl. Catal. A Gen. 502 (2015) 262–270, https://doi.org/10.1016/j.apcata.2015.06.014.
[44] C. Galeano, R. Güttel, M. Paul, P.M. Arnal, A.-H. Lu, F. Schüth, Yolk-shell gold nanoparticles as model materials for support-effect studies example, Chem. - A Eur. J. 17 (2011) 8434–8439, https://doi.org/10.1002/chem.201100318.
[45] G.C. Chinchen, P.J. Denny, J.R. Jennings, M.S. Spencer, K.C. Waugh, Synthesis of methanol part 1, Catal. Kinet. Appl. Catal. 36 (1988) 1–65, https://doi.org/10.1016/S0166-9834(00)80103-7.
[46] S.J. Tauster, S.C. Fung, R.L. Garten, Strong metal-support interactions. Group 8 noble metals supported on TiO_2, J. Am. Chem. Soc. 100 (1978) 170–175, https://doi.org/10.1021/ja00469a029.
[47] S.J. Tauster, S.C. Fung, R.T.K. Baker, J.A. Horsley, Strong interactions in supported-metal catalysts, Science 211 (1981) 1121–1125, https://doi.org/10.1126/science.211.4487.1121.
[48] R. van den Berg, G. Prieto, G. Korpershoek, L.I. van der Wal, A.J. van Bunningen, S. Lægsgaard-Jørgensen, P.E. de Jongh, K.P. de Jong, Structure sensitivity of Cu and CuZn catalysts relevant to industrial methanol synthesis, Nat. Commun. 7 (2016) 20457–20465, https://doi.org/10.1038/ncomms13057.
[49] T. Toupance, M. Kermarec, C. Louis, Metal particle size in silica-supported copper catalysts. Influence of the conditions of preparation and of thermal pretreatments, J. Phys. Chem. B 104 (2000) 965–972, https://doi.org/10.1021/jp993399q.
[50] P. Munnik, M. Wolters, A. Gabrielsson, S.D. Pollington, G. Headdock, J.H. Bitter, P.E. de Jongh, K.P. de Jong, Copper nitrate redispersion to arrive at highly active silica-supported copper catalysts, J. Phys. Chem. C 115 (2011) 14698–14706, https://doi.org/10.1021/jp111778g.
[51] J.A. Menéndez, M.J. Illán-Gómez, C.A. León y León, L.R. Radovic, On the difference between the isoelectric point and the point of zero charge of carbon, Carbon 33 (1995) 1655–1657, https://doi.org/10.1016/0008-6223(95)96817-R.
[52] S. Žalac, N. Kallay, Application of mass titration to the point of zero charge determination, J. Colloid Interface Sci. 149 (1992) 233–240, https://doi.org/10.1016/0021-9797(92)90408-F.
[53] J.S. Noh, J.A. Schwarz, Estimation of the point of zero charge of simple and mixed oxides by mass titration, J. Colloid Interface Sci. 130 (1989) 157–164, https://doi.org/10.1016/S0032-5910(99)00011-X.
[54] J.P. Reymond, F. Kolenda, Estimation of the point of zero charge of simple oxides by mass titration, Powder Technol. 102 (1999) 30–36, https://doi.org/10.1016/S0032-5910(99)00011-X.
[55] A.L. Patterson, The scherrer formula for X-Ray particle size determination, Phys. Rev. 56 (1939) 978–982, https://doi.org/10.1103/PhysRev.56.978.
[56] M. Thommes, K. Kaneko, A.V. Neimark, J.P. Olivier, F. Rodriguez-Reinoso, J. Rouquerol, K.S.W. Sing, Physisorption of gases, with special reference to the evaluation of surface area and pore size distribution (IUPAC Technical Report), Pure Appl. Chem. 87 (2015) 1051–1069, https://doi.org/10.1515/pac-2014-1117.
[57] C.E. Pompe, M. Slagter, P.E. de Jongh, K.P. de Jong, Impact of heterogeneities in silica-supported copper catalysts on their stability for methanol synthesis, J. Catal. 365 (2018) 1–9, https://doi.org/10.1016/j.jcat.2018.06.014.